

Tau PET imaging with ^{18}F -PI-2620 in patients with Alzheimer's disease and healthy controls: a first-in-human study

Authors

Andre Mueller¹, Santiago Bullich¹, Olivier Barret², Jennifer Madonia², Mathias Berndt¹, Caroline Papin^{1,2}, Audrey Perrotin¹, Norman Koglin¹, Heiko Kroth³, Andrea Pfeifer³, Gilles Tamagnan², John P. Seibyl², Kenneth Marek², Susan de Santi⁴, Ludger M. Dinkelborg¹, Andrew W. Stephens¹

¹*Life Molecular Imaging GmbH, Berlin, Germany*

²*Invicro, New Haven, CT, USA*

³*AC Immune SA, Lausanne, Switzerland*

⁴*Life Molecular Imaging Inc, Boston, MA, USA*

Corresponding Author:

Andrew W. Stephens, MD, PhD
Life Molecular Imaging GmbH
Tegeler Straße 6-7, 13353 Berlin, Germany
Email: a.stephens@life-mi.com
Phone: +49-30461124603
Fax: +49-30461124629

First Author:

Andre Mueller, PhD
Life Molecular Imaging GmbH
Tegeler Straße 6-7, 13353 Berlin, Germany
Email: a.mueller@life-mi.com
Phone: +49-30461124607
Fax: +49-30461124629

Word count of the manuscript: 5236

Financial support: Life Molecular Imaging

Short running title: ^{18}F -PI-2620 Tau PET in HC & AD patients

ABSTRACT

¹⁸F-PI-2620 is a positron emission tomography (PET) tracer with high binding affinity for aggregated tau, a key pathologic feature of Alzheimer's disease (AD) and other neurodegenerative disorders. Preclinically, ¹⁸F-PI-2620 binds to both, 3R and 4R tau isoforms. The purpose of this first-in-human study was to evaluate the ability of ¹⁸F-PI-2620 to detect tau pathology in AD patients using PET imaging, as well as to assess its safety and tolerability of this new tau PET tracer. **Methods.** Participants with clinical diagnosis of probable AD and healthy controls (HC) underwent dynamic ¹⁸F-PI-2620 PET imaging for 180 min. ¹⁸F-PI-2620 binding was assessed visually and quantitatively using Distribution Volume Ratios (DVR) estimated from non-invasive tracer kinetics and standardized uptake value ratios (SUVR) measured at different time points post-injection (p.i.) with the cerebellar cortex as the reference region. Time-activity curves and SUVR were assessed in AD and HC, as well as DVR and SUVR correlations and effect size (Cohen's d) over time. **Results.** ¹⁸F-PI-2620 showed peak brain uptake around 5 min p.i. and fast wash-out in non-target regions. In AD subjects, focal asymmetric uptake was evident in temporal and parietal lobes, precuneus, and posterior cingulate cortex. DVR and SUVR in these regions were significantly higher in AD compared to HC. Very low background signal was observed in HC. ¹⁸F-PI-2620 administration was safe and well tolerated. SUVR time activity curves in most regions and subjects achieved a secular equilibrium after 40 min p.i.. A strong correlation ($R^2 > 0.93$) was found between non-invasive DVR and SUVR for all imaging windows starting >30 min p.i.. Similar effect sizes between AD and HC groups were obtained across the different imaging windows. ¹⁸F-PI-2620 uptake in neocortical regions was significantly correlated with the degree of cognitive impairment. **Conclusion.** Initial clinical data obtained in AD and HC demonstrate the high image quality with excellent signal-to-noise of ¹⁸F-PI-2620 PET for imaging tau deposition in AD subjects. Non-invasive quantification using DVR and SUVR for 30 min imaging windows between 30-90 min p.i., e.g. 45-75 min, provides robust and significant discrimination between AD and HC subjects. ¹⁸F-PI-2620 uptake in expected regions is highly correlated to neurocognitive performance.

Key words: Alzheimer's disease, tau, Positron Emission Tomography, PET, PI-2620

INTRODUCTION

Alzheimer's disease (AD) is the leading cause of dementia and a global public health priority (1). Histopathologically, AD is characterized by the presence of extracellular β -amyloid plaques and intracellular hyperphosphorylated tau neurofibrillary tangles. Three ^{18}F -labeled amyloid positron emission tomography (PET) tracers (florbetaben, florbetapir, flutemetamol) underwent histopathology verification in Phase 3 studies and can be used clinically for visualization of β -amyloid neuritic plaques in subjects with cognitive impairment (2-4). More recently several tau PET tracers have entered the clinical development phase (5). Selective tau imaging may not only provide important information on the neurobiology of AD, but may also allow examination of tau accumulation over time and its correlation with cognitive function (5). According to the most recent diagnostic criteria (6), the presence of tau deposition in β -amyloid positive patients together with a clinical evaluation would allow the establishment of a definite diagnosis of AD ante-mortem. Measuring and monitoring tau load and its spread will support the development of disease-modifying therapies.

Beyond its investigation in AD, tau deposition is a key pathology of several other neurodegenerative diseases, including progressive supranuclear palsy, corticobasal degeneration, Pick's disease, chronic traumatic encephalopathy and argyrophilic grain disease. Tau fibrils consist of six different isoforms, with each variant containing a microtubule binding domain comprising three repeat (3R) or four repeat (4R) regions. Different forms are accumulated in different diseases (7). The same protein sequences can also lead to disease-specific folds of tau filaments as in AD and chronic traumatic encephalopathy where all six tau isoforms are present (8,9).

Several tau imaging candidates are currently under investigation and were recently reviewed (10). Currently, most clinical experience was established with AV1451 (flortaucipir, aka T807). Tissue binding analyses with radiolabeled AV1451 demonstrated selective binding to tangles on AD brain tissue but not in other tauopathies (11). A recent AV1451 cross-sectional analysis reported the accuracy for discriminating AD from other neurodegenerative diseases in patients with established diagnoses (12). Further, an AV1451 longitudinal study in AD subjects showed that the amount and location of tau deposition may have implications for both the spread of tau and the cognitive deterioration that occur over an 18-month period (13).

However, AV1451 and other first-generation tau PET tracers are limited by off-target binding in several brain regions, including basal ganglia or choroid plexus which hampers evaluation of some key cortical regions. Off-target binding to monoamine oxidase A has been described for AV1451 (14) or to monoamine

oxidase B for THK5351 (15). The presence of monoamine oxidases within several brain regions limits the interpretation of PET imaging results with these tau tracers. These shortcomings stimulated the investigation of next generation tau PET tracers (16). Among those is ^{18}F -PI-2620, whose discovery, preclinical characterization and binding to both 3R and 4R tau have been recently described (17). The aim of this study was to translate ^{18}F -PI-2620 into humans to obtain clinical proof of concept for PET imaging of cerebral tau pathology and its ability to discriminate AD subjects from healthy controls (HC).

MATERIALS AND METHODS

Subjects

Subjects with probable AD and HC >50 years of age were screened for eligibility. The diagnosis of probable AD was based on the NINCDS/ADRDA (18) and DSM-IV criteria (19), a Clinical Dementia Rating (CDR) (20) score of ≥ 0.5 at screening and Mini-Mental State Examination (MMSE) (21) score ≤ 28 . The main inclusion criteria for HC were no evidence of cognitive impairment as judged by the investigator following the neuropsychological battery which included a CDR score of 0, an AD Assessment Scale-Cognitive Subscale (ADAS-Cog), a MMSE, and no family history of AD or neurological disease associated with dementia. Using an approved β -amyloid PET tracer, a positive β -amyloid PET status (both visual and quantitative analysis) was required for all AD subjects (within 12 months), whereas all HC were β -amyloid negative. β -amyloid PET standardized uptake value ratios (SUVR) and Centiloid values were calculated as described recently (22-24). The study protocol was reviewed and approved by the New England Institutional Review Board and the study was conducted in accordance with the Declaration of Helsinki. All participants (or their legal representatives) provided written informed consent to participate in the study.

Radiotracer Preparation

^{18}F -PI-2620 was synthesized using a GE TRACERlab FX-FN as described previously (17). ^{18}F -PI-2620 was obtained with $16.7 \pm 4.8\%$ radiochemical yield (decay corrected), $>99.5 \pm 1.5\%$ radiochemical purity and molar activity of $152.2 \pm 49.5 \text{ GBq } \mu\text{mol}^{-1}$ at end of synthesis. NeuraceqTM (florbetaben F18 injection) was obtained from SOFIE (Totowa, NJ).

Image Acquisition

All subjects completed a dynamic ^{18}F -PI-2620 PET scan within 30 days of screening. A transmission scan was obtained for attenuation correction. Subjects were administered a single dose of ^{18}F -PI-2620 ($338.7 \pm 20.9 \text{ MBq}$, range 262.7-359.8 MBq) through a venous catheter followed by a 10 mL saline flush.

The mean and standard deviation of the administered mass of PI-2620 was $2.09 \pm 1.61 \mu\text{g}$ (range 0.79-7.70 μg). Immediately following the injection, continuous dynamic brain imaging was performed for up to 180 minutes over two imaging sessions (0-90 min: 6x30 sec, 4x1 min, 4x2 min, 15x5 min; 120-180 min: 12x5 min) on a Siemens ECAT EXACT HR+ camera. β -amyloid PET images were acquired according to the prescribing information using the same PET scanner. A T1-weighted magnetic resonance imaging (MRI) scan was acquired as part of the screening on a Siemens Espree 1.5 Tesla to identify and delineate brain anatomical regions of interest (ROIs).

Image Reconstruction

PET images were reconstructed in a 128 x 128 matrix (zoom=2, pixel size of 2.574 x 2.574 mm) with the ordered subsets expectation maximization algorithm (4 iterations, 16 subsets) and a post hoc Gaussian filter = 5 mm. Corrections for random coincidences, scatter, system dead time and attenuation were performed as provided by the camera manufacturer.

Blood Sampling

Venous blood samples during ^{18}F -PI-2620 PET imaging were collected in 16 subjects (n=7 HC and n=9 AD) from an antecubital venous catheter at pre-injection, and at 5, 10, 30, and 60 min p.i.. Samples were counted to measure activity in the total plasma, whole blood and for parent compound/metabolite analysis. Details on metabolite analysis are provided in the accompanied manuscript (25). A bi-exponential function was used to describe the parent fraction: $p = \alpha e^{-\frac{t-t_0}{\tau_1}} + (100 - \alpha)e^{-\frac{t-t_0}{\tau_2}}$, where p is parent fraction in percent, t is time after injection in minutes, and α , τ_1 , τ_2 and t_0 the model parameters.

Image Analysis and Quantification

Reconstructed PET images were processed using SPM12 software (<http://www.fil.ion.ucl.ac.uk/spm/doc/>) including motion correction and co-registration onto the subject's MRI. The MRI was segmented into grey matter, white matter and cerebrospinal fluid. Subsequently, the MRI was normalized into the standard MNI (Montreal Neurological Institute) template and the same transformation was applied to the co-registered PET images and grey matter probability maps. ROIs were defined as the intersection between the standard Automated Anatomic Labeling (AAL) volume of interest template (26) and the normalized grey matter segmentation thresholded at a probability level of 0.2. Cortical ROIs were extracted from the AAL template including amygdala, hippocampus, parahippocampus, fusiform gyrus, inferior lateral temporal, superior lateral temporal, occipital, parietal, posterior cingulate cortices, thalamus, striatum and cerebellar grey

matter. ROIs for pallidum (extracted from AAL atlas), choroid plexus (posterior part, manually drawn) and subcortical white matter (centrum semiovale, manually drawn) were delineated on the standard MNI space and applied to all subjects. Cerebellar grey matter (CGM) excluding vermis and anterior lobe surrounding the vermis was used as the reference region. Average activity concentration (kBq/mL) at each time point was determined for each ROI and time-activity curves were generated.

Time-activity curves were analyzed using PMOD 3.7 software package (PMOD Technologies, Zurich, Switzerland). The Distribution Volume Ratios (DVR) was estimated using non-invasive Logan graphical plot (NI-LGA) ($t^*=20$ min, $k_2'=0.22$ min⁻¹) and CGM as reference region (27). SUVR at different time points was calculated as the ratio of the mean activity concentration in the target ROI to the mean activity concentration in the reference region ROI (CGM). SUVR was determined at six 30-min imaging windows (20-50, 30-60, 45-75, 60-90, 120-150, and 150-180 min p.i.) by averaging the SUVR at different time points within each imaging window.

Safety and Tolerability

Safety and tolerability were assessed at all study visits and included blood and urine samples for laboratory tests, electrocardiograms, physical and clinical examinations and assessments for adverse events.

Statistical Analysis

SUVR data were compared between AD and HC groups in different ROIs using Mann-Whitney U test. The effect size between AD and HC subjects was assessed by means of Cohen's d. DVR and SUVR measures were compared by means of linear regression.

RESULTS

Subject Demographics

A total of 10 HC and 12 AD subjects were included in this analysis. Subject demographics and β -amyloid PET status are presented in Table 1. Mean age was 59.2 ± 7.8 years for HC and 68.5 ± 9.8 years for AD subjects. Mean MMSE and score ranges in HC and AD group were 29 [range 26-30] and 20.5 [range 8-28] respectively. In HCs, the mean amyloid-PET global SUVR was 1.00 ± 0.04 [range 0.91-1.04] and mean Centiloid 2.05 ± 6.65 [range -16-5], the AD cases had a mean SUVR of 1.66 ± 0.15 [range 1.47-1.99] and mean Centiloid of 101 ± 21 [range 71-150].

Safety and Tolerability

There were no adverse or clinically detectable pharmacologic effects from ^{18}F -PI-2620 administration in any of the 22 subjects. No clinically significant changes were observed in vital signs, laboratory values or electrocardiograms.

Visual Assessment

In HCs, no areas of specific ^{18}F -PI-2620 cerebral uptake were identified visually (Fig. 1) and a consistent pattern of initial uptake and wash-out was observed throughout. In AD subjects, tracer accumulation was identified in cortical regions involving mainly temporal and parietal lobes, precuneus and posterior cingulate cortex. Two AD subjects showed low tracer retention (#18, #19). Prior to 20 min post-injection (p.i.) increased non-displaceable uptake (vascular component) was observed, while late scans were noisier with a complete wash-out of the tracer (150-180 min). Tracer retention was observed in the pineal gland in one aged HC (#2). ^{18}F -PI-2620 uptake in the cerebellar vermis was observed in 10 subjects (#1, #3, #5, #7-10, #12, #19, #21). Variable activity was observed in the substantia nigra of most of the HC and AD subjects. No binding higher than the uptake in the reference region was found in the choroid plexus. Extracerebral activity of the tracer was common in the retina and in the venous sinus in early scans. Variable uptake was also seen in the skull, which was not consistent with defluorination. One case showed meningeal uptake. Anterior maxillary sinuses also showed prominent uptake in some cases. No signs of defluorination (i.e. tracer accumulation in bone) were observed. A comparison of amyloid PET and ^{18}F -PI-2620 PET images from a single subject is shown in Figure 2.

Blood Sampling

Venous plasma analysis demonstrated fast clearance of ^{18}F -PI-2620 from the blood. The metabolite-pattern from venous blood was not different to arterial blood, which is described in the accompanying manuscript (25). Unmetabolized parent compound in plasma was reduced to $50.5 \pm 12.1\%$ at 10 min p.i., $21.3 \pm 8.7\%$ at 30 min p.i. and $14.4 \pm 4.9\%$ at 60 min p.i. (Supplemental Fig. 1).

Time-Activity Curves and SUVR over Time

In all subjects, time-activity curves reached a peak around 5 min after injection. In HCs, a rapid and uniform wash-out was observed for the cortex and reference region (CGM). In AD subjects, wash-out was slower compared to HCs in those areas where an accumulation of neurofibrillary tangles can be expected. Both HC and AD subjects displayed rapid and similar clearance of the tracer in the reference region and across

brain regions devoid of tau. Visual inspection of the SUVR curves revealed that SUVR stabilization was achieved around 40 min p.i. for most subjects (n=18) while SUVR continued to increase in some AD subjects (n=4) until the end of the imaging window at 180 min p.i. without reaching secular equilibrium. Representative time-activity and SUVR curves from 1 HC and 2 AD cases are shown in Figure 3. Strong correlation was found between the DVR obtained from the NI-LGA and SUVR for all imaging windows starting 30 min p.i. ($R^2 > 0.94$) (Fig. 4), with increasing slope due to rising SUVR at time points after 60 min p.i..

Quantitative Analyses and Effect Size

^{18}F -PI-2620 uptake in different cortical regions is shown as SUVR box plots in Figure 5 for all AD and HC subjects. AD subjects showed generally higher SUVR than HCs with a variable degree in individual regions. Similar results were obtained from the analyses of the DVR using the NI-LGA and SUVRs at different imaging windows (Supplemental Table 1). Statistically significant differences between AD and HC were also found using maximum SUVR at different imaging windows (Supplemental Fig. 2). As shown in Table 2, the largest effect sizes to discriminate between AD and HCs using SUVR at 45-75 min p.i. were obtained for the fusiform gyrus ($d=2.45$), inferior temporal ($d=2.35$) and occipital cortices ($d=2.06$). DVR and SUVR analyses of subcortical regions did not show statistically significant differences between AD and HCs in most regions and time points. However, increased signal was observed in the pallidum, subcortical white matter and striatum in SUVR at early time points and only in the pallidum in DVR analysis (Supplemental Table 2).

Correlation with Cognition

A correlation analysis of ^{18}F -PI-2620 uptake in individual brain regions and ADAS-Cog is shown in Figure 6. Significant correlation of ^{18}F -PI-2620 SUVR at 45-75min p.i. with the ADAS-Cog measurements was observed for the following regions: fusiform gyrus, inferior lateral temporal, superior lateral temporal, occipital, and parietal cortices, with correlation coefficients between 0.45 and 0.54. Significant correlation with MMSE was found in the same regions but with lower correlation coefficients (Supplemental Fig. 3).

DISCUSSION

The present study showed accumulation of ^{18}F -PI-2620 in regions known to have tau deposition in β -amyloid positive clinically probable AD subjects. HC subjects showed very low ^{18}F -PI-2620 accumulation and AD subjects could be clearly distinguished. As such, the ^{18}F -PI-2620 human data obtained in this study

are consistent with the tracer characteristics described preclinically in terms of target binding, pharmacokinetic and off-target binding (17). This is an improvement compared to the first-generation tau agents, in which off-target binding may confound the visual and quantitative assessments and may limit their ability to specifically image tau pathology, for example in the mesial-temporal regions.

Highest uptake of ^{18}F -PI-2620 was observed in the fusiform gyrus, inferior temporal and occipital regions in AD subjects. The spatial distribution observed here parallels neuropathological data reporting tau spread from the entorhinal cortex, through inferior-lateral temporal and medial parietal areas to the neocortex (28). The inter-subject variability in the distribution and density of tracer uptake in AD cases observed in this study is consistent with previous tau PET imaging studies (12,29-31).

Both HC and AD subjects showed high initial brain uptake and rapid clearance of ^{18}F -PI-2620 in the reference region and across brain regions devoid of tau. The wash-out was slower in AD in areas where an accumulation of neurofibrillary tangles can be expected compared to HC. ^{18}F -PI-2620 shows fastest tracer clearance pattern described for tau PET agents to date. Rapid and complete wash-out from the cerebellar reference regions provides the opportunity for an early and robust SUVR assessment. SUVR curves over time suggest a plateau occurring around 40 min p.i. in most of the AD subjects and regions analysed, with resulting SUVR up to 4.0 in abnormal regions, while HC demonstrated low and stable SUVRs generally around 1.0 in the same regions over time. For some patients, secular equilibrium was not reached over the 180 min acquisition period resulting in a continued increase of the signal as also reported for another tau PET tracer (32). Measurable signal was observed in the basal ganglia of AD subjects by group analysis. This was driven by three subjects with increased uptake in the basal ganglia and also significant neocortical tracer uptake (#13, #17, #20). Two recent autopsy studies have shown tau deposition in basal ganglia of subjects with advanced AD (Braak V/VI) (33,34). As such, uptake in subcortical regions in advanced AD is not unexpected and should not occur in the absence of significant neocortical uptake.

The kinetics of tracer uptake described in this study indicate that ^{18}F -PI-2620 has a broad imaging window starting as early as 30 min p.i.. The strong correlation and linearity observed between SUVR and DVR indicate that SUVR is a good proxy for DVR. PET scans performed within the time frame of 30 to 90 min provide excellent quantification accuracy with strong correlation between SUVR and full tracer kinetic quantification, optimal effect size and visual assessment in AD as described in the accompanying manuscript in more detail (25). For example, scans acquired at 45-75min p.i. provide a good compromise and can be recommended for static acquisitions.

A significant correlation between cognitive measurements (ADAS-Cog and MMSE) and tracer uptake in neocortical ROIs was found. A trend between ADAS-Cog and tracer uptake in mesial-temporal regions was observed. However, given the lower tau accumulation in these regions and the small sample size, it did not reach statistical significance. This is consistent with the hypothesis that tau accumulation begins in mesial-temporal regions but does not reach high levels in these regions. Rather after a certain level of accumulation tau may cross the temporal sulcus into fusiform gyrus and inferior temporal lobe. Of note, the statistical significance of the correlation between neocortical regions and cognition was lost when the HC were removed from the analysis, probably as a result of the very small number of remaining subjects. The ADAS-Cog and MMSE are global measurements of cognition; episodic memory tests and more detailed neuropsychological instruments may provide more insights into the correlation between tau load in specific brain regions and specific cognitive functions.

Limitations of this study are the small number of subjects, the mean age difference between subject groups, and the cross-sectional aspect of the study. These limitations need to be addressed in future studies, longitudinal follow-up and larger subject groups.

CONCLUSION

Results from this first-in-human study showed increased uptake of ^{18}F -PI-2620 in AD compared to HC. The tracer is safe and well tolerated. Comparing β -amyloid negative HC to AD subjects with amyloid positivity and different levels of cognitive impairment, prominent and significant tracer uptake was observed in regions expected to accumulate abnormal tau aggregates. Notable with ^{18}F -PI-2620 is the very fast brain uptake and clearance from non-target regions, which allows for imaging windows around 60 min. SUVR provides a reasonable approximation of DVR, especially before 90 min and the rapid clearance allows the possibility of full dynamic imaging in a clinically relevant time period. Additional studies with larger numbers of subjects and involving other tauopathies are needed to further characterize and validate this tracer.

DISCLOSURES

Andre Mueller, Santiago Bullich, Mathias Berndt, Norman Koglin, Caroline Papin, Susan de Santi, Ludger M. Dinkelborg and Andrew W. Stephens are employed by Life Molecular Imaging, who funded the clinical study. Audrey Perrotin serves as consultant for Life Molecular Imaging. Olivier Barret, Jennifer Madonia, Caroline Papin, Gilles Tamagnan, John P. Seibyl, Kenneth Marek were employed by MNI, Molecular Neuroimaging, LLC, now Invicro, who were contracted by Life Molecular Imaging to conduct the clinical study. Andrea Pfeifer and Heiko Kroth are employed by AC Immune and hold shares of AC Immune. No other potential conflict of interest relevant to this article was reported.

ACKNOWLEDGMENTS

The authors thank all patients, their caregivers, and the healthy volunteers who participated in this trial. We are also grateful to the chemistry and clinical translational research staff at Invicro (formerly MNI) for their excellent technical assistance.

KEY POINTS

QUESTION: Does ^{18}F -PI-2620 show suitable brain uptake and clearance in humans, and retention in Alzheimer disease patients?

PERTINENT FINDINGS: Clinical proof of concept was obtained for ^{18}F -PI-2620 for visualizing areas with suspected tau pathology in AD patients with fast clearance from non-affected regions, high image quality and low off-target binding. ^{18}F -PI-2620 uptake was highly correlated to cognitive function.

IMPLICATIONS FOR PATIENT CARE: ^{18}F -PI-2620 may help to better track and understand tau pathophysiology, disease progression and improve diagnosis in neurocognitive impairment.

REFERENCES

1. WHO. Global action plan on the public health response to dementia 2017–2025. 2017.
2. Clark CM, Schneider JA, Bedell BJ, et al. Use of florbetapir-PET for imaging beta-amyloid pathology. *JAMA*. 2011;305:275-283.
3. Curtis C, Gamez JE, Singh U, et al. Phase 3 trial of flutemetamol labeled with radioactive fluorine 18 imaging and neuritic plaque density. *JAMA Neurol*. 2015;72:287-294.
4. Sabri O, Sabbagh MN, Seibyl J, et al. Florbetaben PET imaging to detect amyloid beta plaques in Alzheimer's disease: phase 3 study. *Alzheimers Dement*. 2015;11:964-974.
5. Villemagne VL, Dore V, Burnham SC, Masters CL, Rowe CC. Imaging tau and amyloid-beta proteinopathies in Alzheimer disease and other conditions. *Nat Rev Neurol*. 2018;14:225-236.
6. Jack CR, Jr., Bennett DA, Blennow K, et al. NIA-AA Research Framework: Toward a biological definition of Alzheimer's disease. *Alzheimers Dement*. 2018;14:535-562.
7. Goedert M, Spillantini MG, Jakes R, Rutherford D, Crowther RA. Multiple isoforms of human microtubule-associated protein tau: sequences and localization in neurofibrillary tangles of Alzheimer's disease. *Neuron*. 1989;3:519-526.
8. Falcon B, Zivanov J, Zhang W, et al. Novel tau filament fold in chronic traumatic encephalopathy encloses hydrophobic molecules. *Nature*. 2019;568:420-423.
9. Fitzpatrick AWP, Falcon B, He S, et al. Cryo-EM structures of tau filaments from Alzheimer's disease. *Nature*. 2017;547:185-190.
10. Schöll M, Maass A, Mattsson N, et al. Biomarkers for tau pathology. *Mol Cell Neurosci*. 2019;97:18-33.
11. Marquie M, Normandin MD, Vanderburg CR, et al. Validating novel tau positron emission tomography tracer [F-18]-AV-1451 (T807) on postmortem brain tissue. *Ann Neurol*. 2015;78:787-800.
12. Ossenkoppele R, Rabinovici GD, Smith R, et al. Discriminative accuracy of [18F]flortaucipir positron emission tomography for Alzheimer disease vs other neurodegenerative disorders. *JAMA*. 2018;320:1151-1162.
13. Pontecorvo MJ, Devous MD, Kennedy I, et al. A multicentre longitudinal study of flortaucipir (18F) in normal ageing, mild cognitive impairment and Alzheimer's disease dementia. *Brain*. 2019;142:1723-1735.

14. Vermeiren C, Motte P, Viot D, et al. The tau positron-emission tomography tracer AV-1451 binds with similar affinities to tau fibrils and monoamine oxidases. *Mov Disord*. 2018;33:273-281.
15. Ng KP, Pascoal TA, Mathotaarachchi S, et al. Monoamine oxidase B inhibitor, selegiline, reduces (18)F-THK5351 uptake in the human brain. *Alzheimers Res Ther*. 2017;9:25.
16. Leuzy A, Chiotis K, Lemoine L, et al. Tau PET imaging in neurodegenerative tauopathies—still a challenge. *Molecular Psychiatry*. 2019;24:1112-1134.
17. Kroth H, Oden F, Molette J, et al. Discovery and preclinical characterization of [(18)F]PI-2620, a next-generation tau PET tracer for the assessment of tau pathology in Alzheimer's disease and other tauopathies. *Eur J Nucl Med Mol Imaging*. 2019;46:2178-2189.
18. McKhann G, Drachman D, Folstein M, Katzman R, Price D, Stadlan EM. Clinical diagnosis of Alzheimer's disease: report of the NINCDS-ADRDA Work Group under the auspices of Department of Health and Human Services Task Force on Alzheimer's Disease. *Neurology*. 1984;34:939-944.
19. American Psychiatric Association. *Diagnostic criteria from DSM-IV*. Washington, D.C.: The Association; 1994:123-164.
20. Morris JC. The Clinical Dementia Rating (CDR): current version and scoring rules. *Neurology*. 1993;43:2412-2414.
21. Folstein MF, Robins LN, Helzer JE. The Mini-Mental State Examination. *Arch Gen Psychiatry*. 1983;40:812.
22. Klunk WE, Koeppe RA, Price JC, et al. The Centiloid Project: standardizing quantitative amyloid plaque estimation by PET. *Alzheimers Dement*. 2015;11:1-15 e11-14.
23. Navitsky M, Joshi AD, Kennedy I, et al. Standardization of amyloid quantitation with florbetapir standardized uptake value ratios to the Centiloid scale. *Alzheimers Dement*. 2018;14:1565-1571.
24. Rowe CC, Dore V, Jones G, et al. (18)F-Florbetaben PET beta-amyloid binding expressed in Centiloids. *Eur J Nucl Med Mol Imaging*. 2017;44:2053-2059.
25. Bullich S, Barret O, Constantinescu C, et al. Evaluation of dosimetry, quantitative methods and test-retest variability of 18F-PI-2620 PET for the assessment of tau deposits in the human brain. *J Nucl Med*. ????:??:??-??.
26. Tzourio-Mazoyer N, Landeau B, Papathanassiou D, et al. Automated anatomical labeling of activations in SPM using a macroscopic anatomical parcellation of the MNI MRI single-subject brain. *Neuroimage*. 2002;15:273-289.

27. Logan J. Graphical analysis of PET data applied to reversible and irreversible tracers. *Nucl Med Biol.* 2000;27:661-670.
28. Braak H, Alafuzoff I, Arzberger T, Kretschmar H, Del Tredici K. Staging of Alzheimer disease-associated neurofibrillary pathology using paraffin sections and immunocytochemistry. *Acta Neuropathol.* 2006;112:389-404.
29. Jack CR, Jr., Wiste HJ, Schwarz CG, et al. Longitudinal tau PET in ageing and Alzheimer's disease. *Brain.* 2018;141:1517-1528.
30. Johnson KA, Schultz A, Betensky RA, et al. Tau positron emission tomographic imaging in aging and early Alzheimer disease. *Ann Neurol.* 2016;79:110-119.
31. Pontecorvo MJ, Devous MD, Sr., Navitsky M, et al. Relationships between flortaucipir PET tau binding and amyloid burden, clinical diagnosis, age and cognition. *Brain.* 2017;140:748-763.
32. Guehl NJ, Wooten DW, Yokell DL, et al. Evaluation of pharmacokinetic modeling strategies for in-vivo quantification of tau with the radiotracer [(18)F]MK6240 in human subjects. *Eur J Nucl Med Mol Imaging.* 2019;46:2099-2111.
33. Hamasaki H, Honda H, Suzuki SO, et al. Tauopathy in basal ganglia involvement is exacerbated in a subset of patients with Alzheimer's disease: The Hisayama study. *Alzheimers Dement (Amst).* 2019;11:415-423.
34. Zhu K, Wang X, Sun B, et al. Primary age-related tauopathy in human subcortical nuclei. *Front Neurosci.* 2019;13:529.

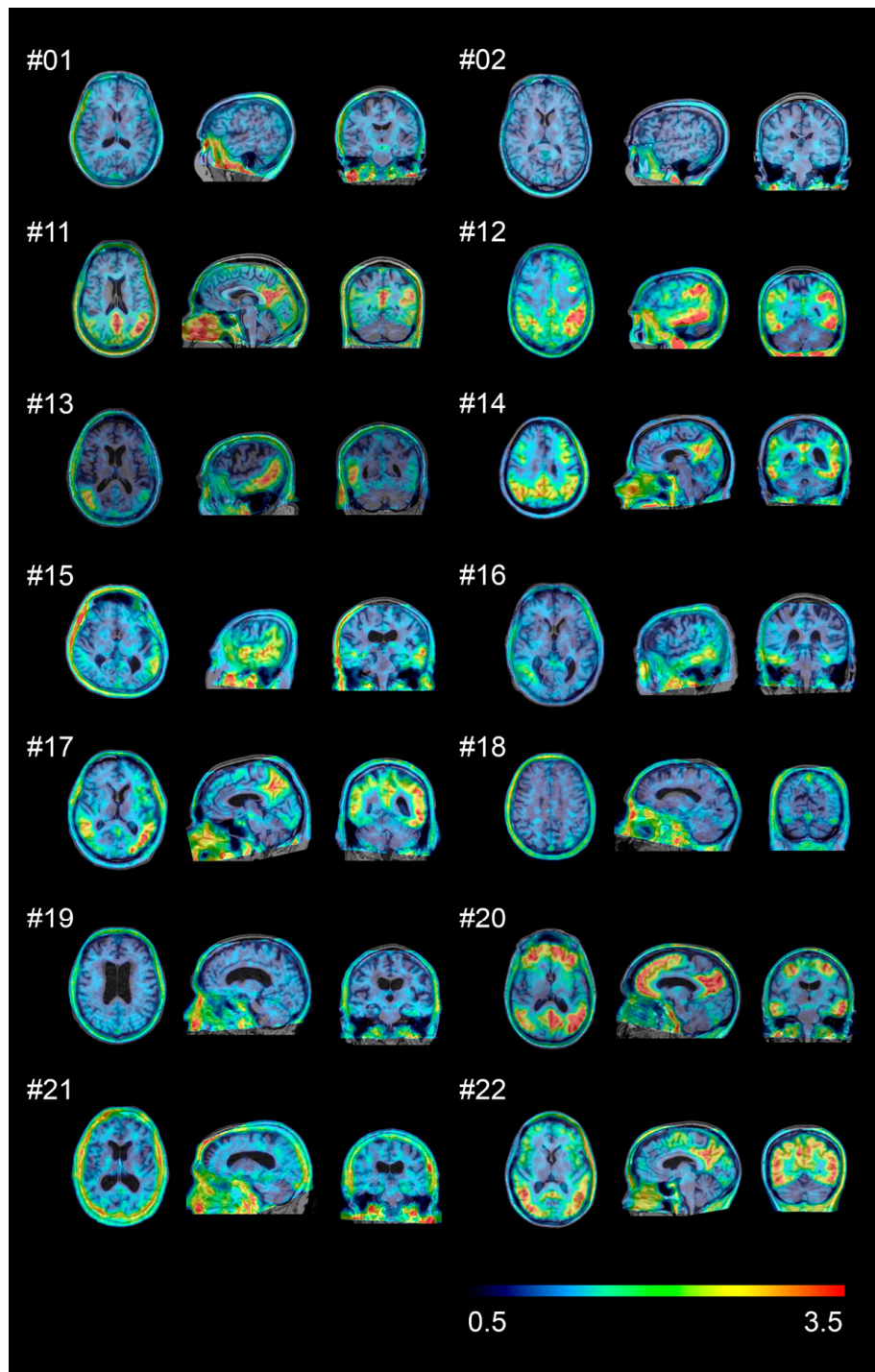


FIGURE 1. ^{18}F -PI-2620 SUVR images (45-75 min) for two representative HCs are shown in the upper row and below for all AD patients (cases #11-#22). Images were normalized to the cerebellar grey matter and co-registered to the subject's MRI.

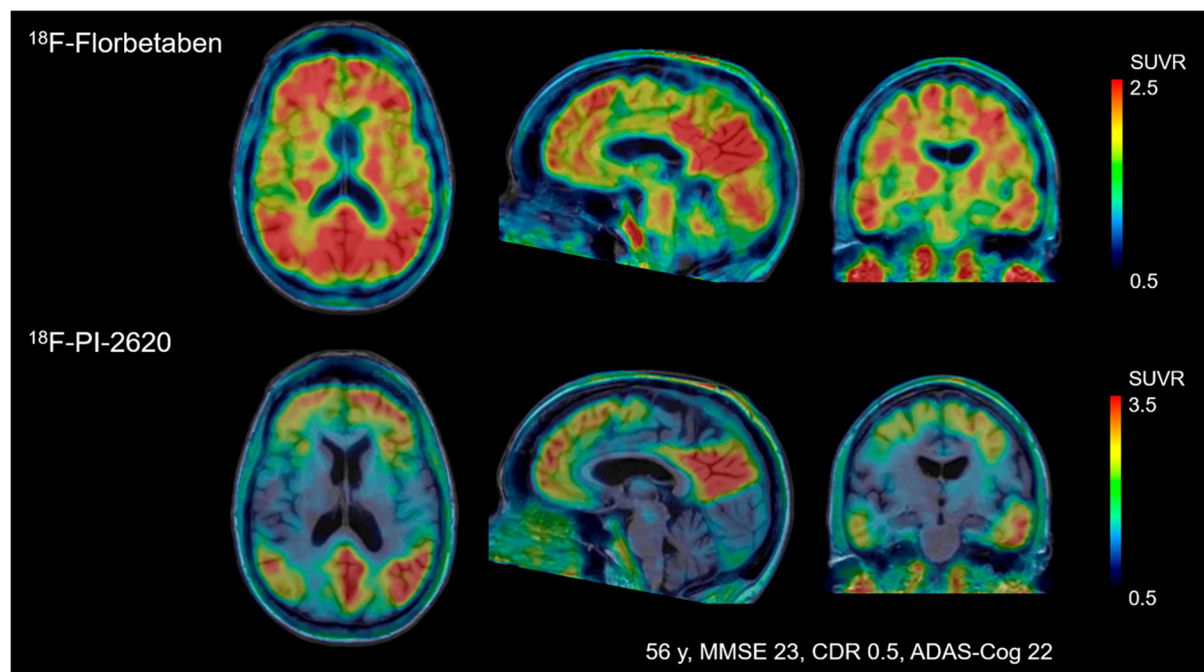


FIGURE 2. Comparison of florbetaben amyloid-PET and ¹⁸F-PI-2620 tau PET obtained in the same subject. Images were normalized to the cerebellar grey matter and co-registered to the subject's MRI.

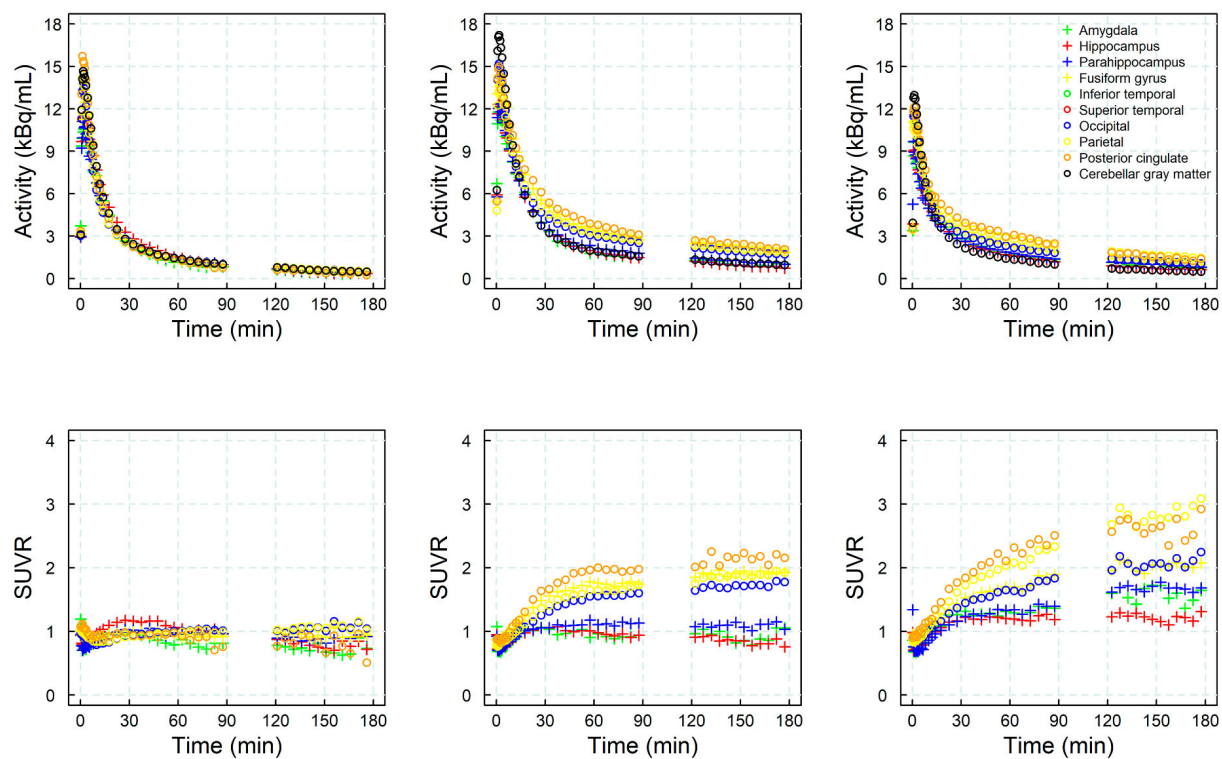


FIGURE 3. Illustrative time–activity curves (top row) and SUVRs (bottom row) from selected brain regions in one HC (left column, subject #4) and two AD subjects (center, subject #14, and right column, subject #17).

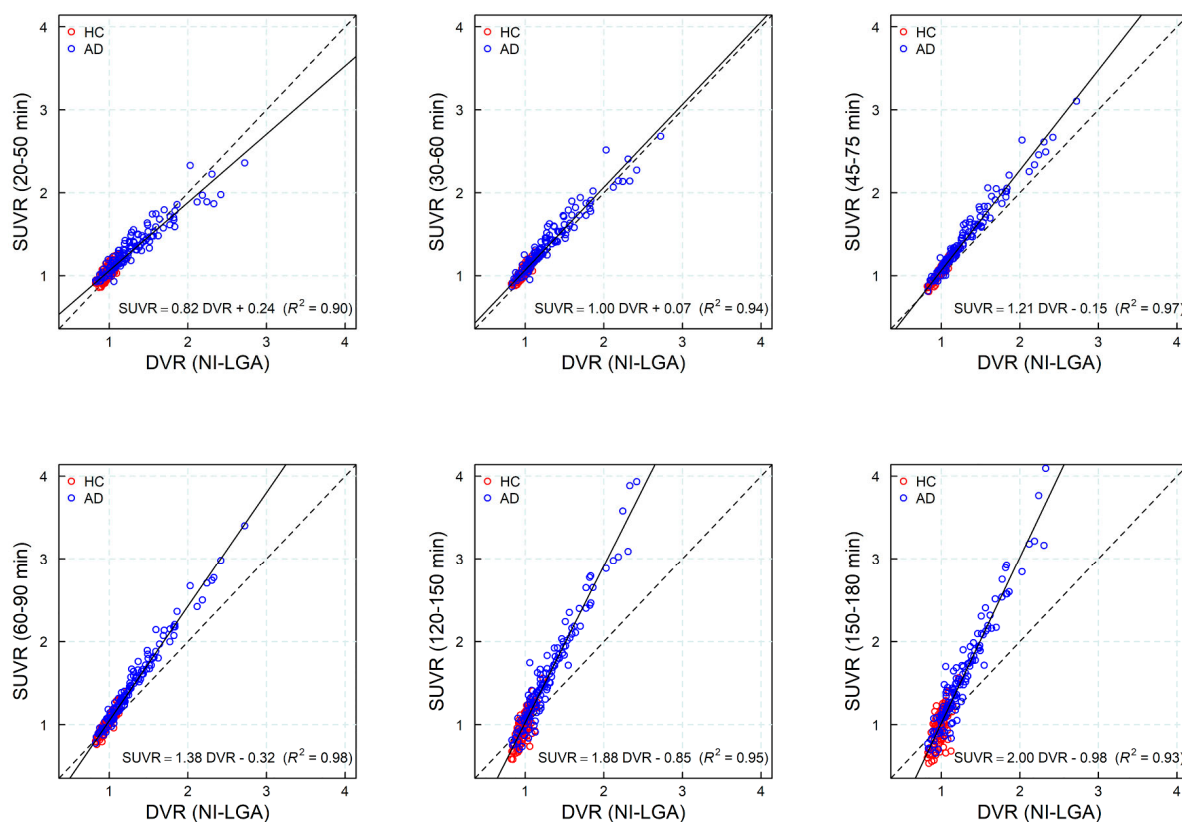


FIGURE 4. Scatter plot and regression line (continuous line) of the SUVR at different imaging windows versus the DVR from the NI-LGA. Dashed line corresponds to the identity line.

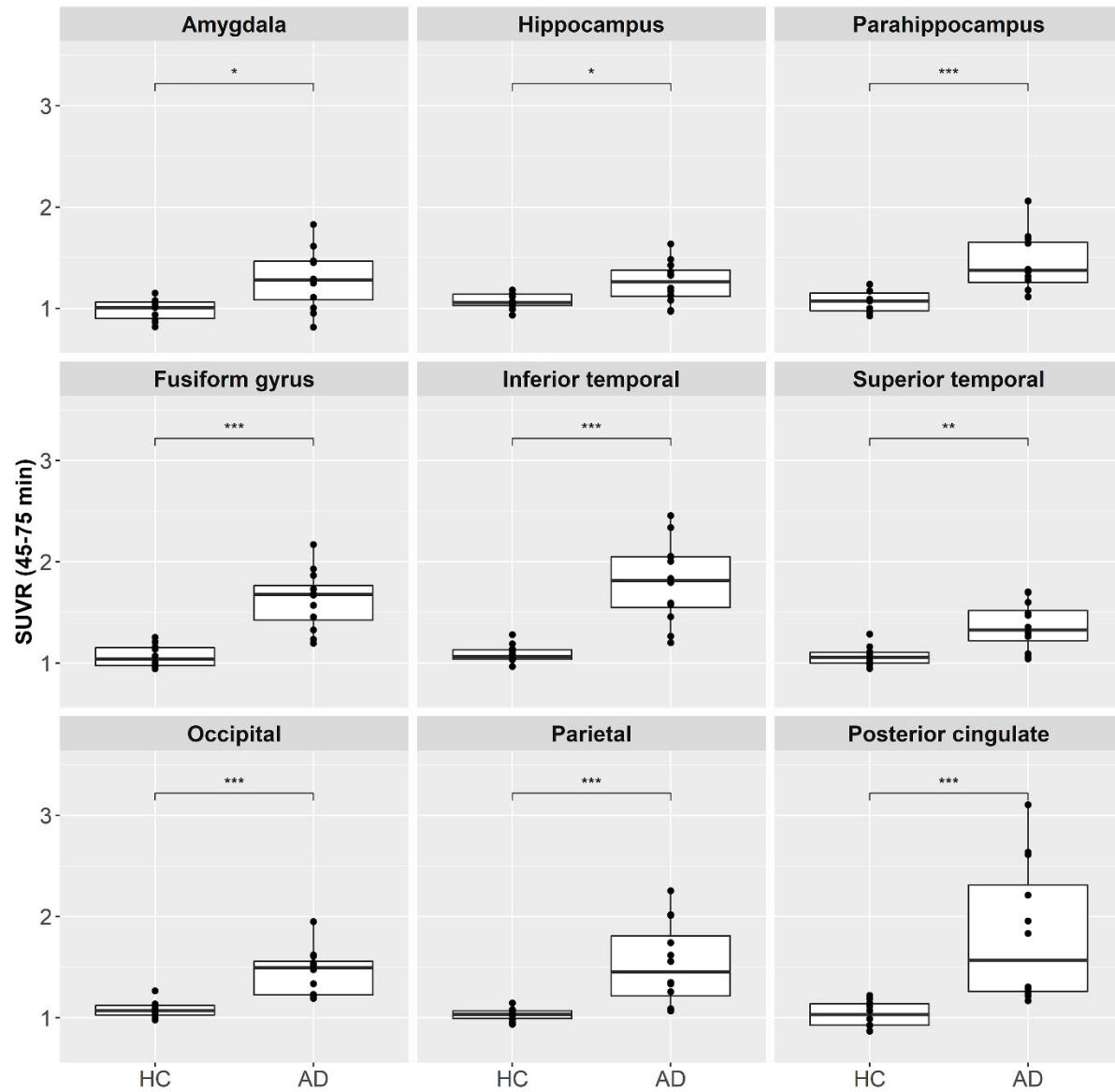


FIGURE 5. Boxplot of SUVR (45-75 min) at each diagnosis group for different brain regions.
 (* ($p \leq 0.05$), ** ($p \leq 0.01$), ***: ($p \leq 0.001$))

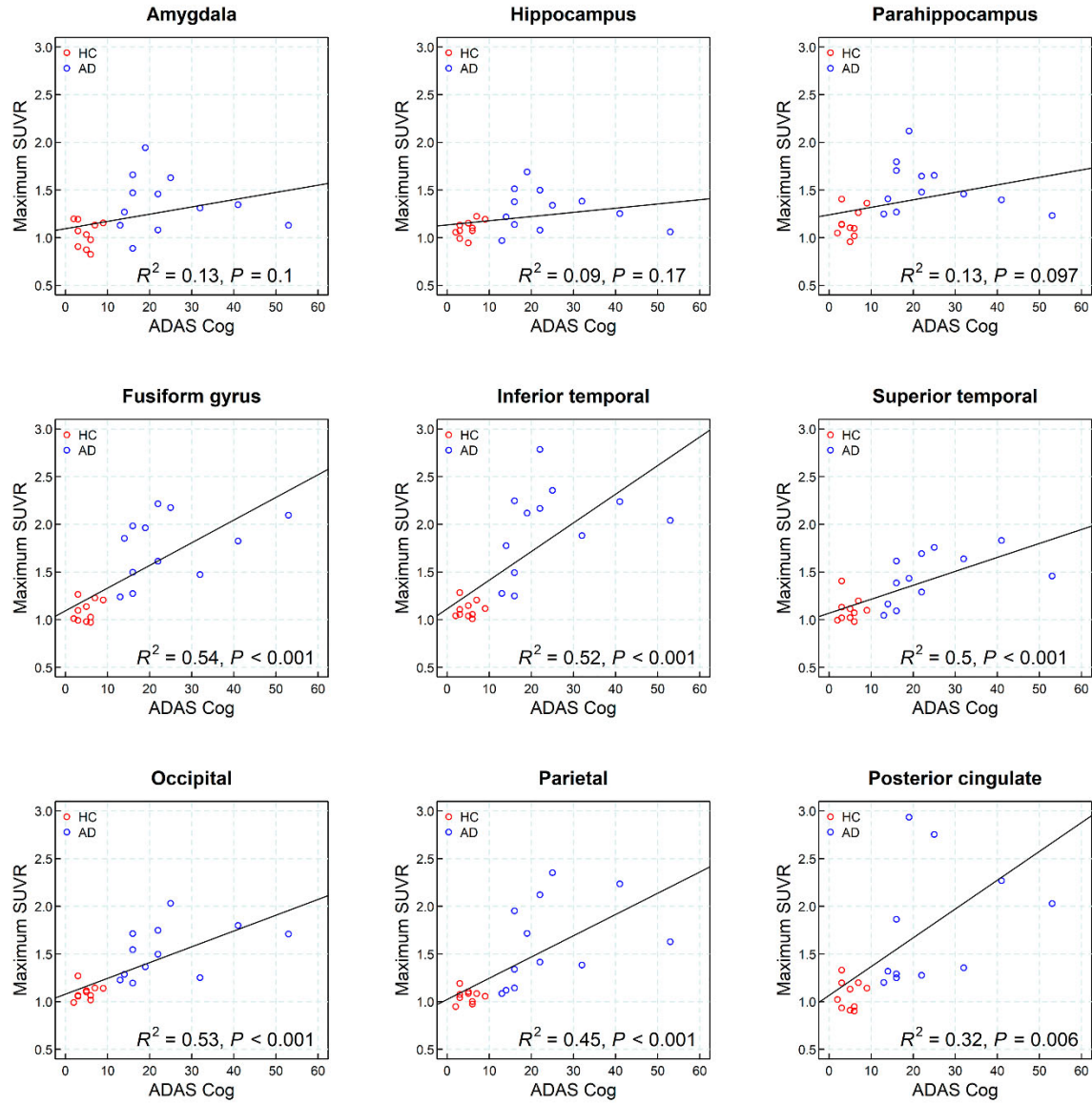


FIGURE 6. Correlation analysis of ^{18}F -Pi-2620 uptake at 45-75 min p.i. in individual brain regions (maximum SUVR from the left or the right hemisphere) and ADAS-Cog.

TABLE 1. Demographics of subjects enrolled in the study.

Subject ID	Gender	Age (yrs)	Cohort	Injected dose (MBq)	β -amyloid status (visual)	β -amyloid global SUVR*	β -amyloid Centiloid score†	ADAS-Cog Score	CDR Score	MMS E Score
1	female	65	HC	341.5	Negative	1.00	-2	5	0	29
2	female	75	HC	339.7	Negative	0.91	-16	7	0	30
3	male	61	HC	333.4	Negative	1.00	-1	3	0	30
4	male	51	HC	347.8	Negative	1.02	2	6	0	29
5	female	53	HC	353.4	Negative	1.03	3	5	0	29
6	male	56	HC	347.1	Negative	0.98	-5	2	0	26
7	male	50	HC	332.6	Negative	1.04	5	6	0	28
8	male	66	HC	353.4	Negative	1.01	0	9	0	30
9	male	60	HC	299.0	Negative	1.03	4	3	0	30
10	female	55	HC	262.7	Negative	0.94	-10	3	0	29
11	male	58	AD	346.3	Positive	1.99	150	19	0.5	20
12	female	63	AD	333.4	Positive	1.67	101	16	0.5	28
13	male	71	AD	335.2	Positive	1.66	100	22	0.5	20
14	female	63	AD	339.3	Positive	1.83	126	53	2	8
15	male	70	AD	352.2	Positive	1.66	100	32	0.5	22
16	male	80	AD	351.1	Positive	1.53	79	14	0.5	17
17	male	72	AD	343.7	Positive	1.73	111	41	2	8
18	male	77	AD	336.7	Positive	1.62‡	102	16	0.5	26
19	male	76	AD	347.4	Positive	1.47	71	13	1	27
20	female	56	AD	359.6	Positive	1.71	108	22	0.5	23
21	male	83	AD	349.3	Positive	1.47‡	76	16	0.5	23
22	female	53	AD	348.2	Positive	1.57	85	25	0.5	23

* SUVR calculated as described by Klunk (22)

† Conversion to Centiloid was performed as follows: CL=153.4 SUVR_{FBB} – 154.9 (24); CL=175 SUVR_{FBB} – 182 (23)

‡ Subject scanned with florbetapir

TABLE 2. Effect size (Cohen’s d) for DVR and SUVR comparing AD subjects and HC. Three largest d values for each method and imaging window are marked in bold

	NI-LGA	SUVR					
	DVR	20-50 min	30-60 min	45-75 min	60-90 min	120-150 min	150- 180 min
Amygdala	1.52	1.28	1.28	1.35	1.34	1.69	1.74
Hippocampus	1.09	0.68	0.89	1.17	1.36	2.28	2.20
Parahippocampus	1.91	1.69	1.71	1.68	1.68	2.10	2.16
Fusiform gyrus	2.10	2.59	2.59	2.45	2.35	2.16	2.10
Inferior temporal	2.08	2.70	2.55	2.35	2.22	2.03	1.98
Superior temporal	1.39	1.62	1.63	1.57	1.42	1.48	1.50
Occipital	1.77	2.18	2.13	2.06	1.92	1.72	1.66
Parietal	1.46	1.80	1.75	1.65	1.56	1.44	1.38
Posterior cingulate	1.34	1.59	1.56	1.54	1.49	1.24	1.32

SUPPLEMENTAL DATA

SUPPLEMENTAL TABLE 1. DVR and SUVR values (mean \pm SD) at different imaging windows for the amygdala, hippocampus, parahippocampus, fusiform gyrus, inferior temporal, superior temporal, occipital, parietal, and posterior cingulate.

		NI-LGA	SUVR					
		DVR	20-50 min	30-60 min	45-75 min	60-90 min	120-150 min	150- 180 min
Amygdala	HC	0.95 \pm 0.07	1.05 \pm 0.07	1.03 \pm 0.09	0.99 \pm 0.11	0.97 \pm 0.13	0.93 \pm 0.19	0.91 \pm 0.20
	AD	1.18 \pm 0.19**	1.28 \pm 0.23 (n.s)	1.29 \pm 0.26*	1.29 \pm 0.29*	1.31 \pm 0.32*	1.42 \pm 0.35**	1.41 \pm 0.34*
Hippocampus	HC	1.00 \pm 0.05	1.16 \pm 0.06	1.14 \pm 0.07	1.07 \pm 0.08	1.01 \pm 0.09	0.87 \pm 0.10	0.81 \pm 0.11
	AD	1.12 \pm 0.14*	1.26 \pm 0.18 (n.s)	1.27 \pm 0.20 (n.s)	1.26 \pm 0.20*	1.24 \pm 0.21*	1.23 \pm 0.19***	1.19 \pm 0.21**
Parahippocampus	HC	0.99 \pm 0.08	1.06 \pm 0.07	1.07 \pm 0.08	1.07 \pm 0.11	1.07 \pm 0.14	1.07 \pm 0.18	1.03 \pm 0.18
	AD	1.29 \pm 0.20**	1.34 \pm 0.21 ***	1.40 \pm 0.25***	1.46 \pm 0.29***	1.50 \pm 0.32**	1.65 \pm 0.34***	1.67 \pm 0.36***
Fusiform gyrus	HC	1.02 \pm 0.07	1.08 \pm 0.08	1.08 \pm 0.09	1.07 \pm 0.11	1.05 \pm 0.13	1.04 \pm 0.14	1.02 \pm 0.14
	AD	1.45 \pm 0.27***	1.49 \pm 0.20***	1.57 \pm 0.24***	1.63 \pm 0.29***	1.68 \pm 0.34***	1.82 \pm 0.47***	1.84 \pm 0.51***
Inferior temporal	HC	1.04 \pm 0.06	1.07 \pm 0.07	1.08 \pm 0.08	1.09 \pm 0.09	1.09 \pm 0.10	1.11 \pm 0.10	1.11 \pm 0.10
	AD	1.61 \pm 0.37***	1.59 \pm 0.25***	1.70 \pm 0.32***	1.80 \pm 0.40***	1.88 \pm 0.47***	2.15 \pm 0.68***	2.21 \pm 0.74***
Superior temporal	HC	1.02 \pm 0.06	1.02 \pm 0.08	1.05 \pm 0.09	1.07 \pm 0.10	1.09 \pm 0.10	1.09 \pm 0.08	1.09 \pm 0.07
	AD	1.26 \pm 0.23**	1.24 \pm 0.17**	1.30 \pm 0.19**	1.36 \pm 0.23**	1.40 \pm 0.28**	1.60 \pm 0.46**	1.64 \pm 0.49***
Occipital	HC	1.02 \pm 0.06	1.03 \pm 0.07	1.06 \pm 0.07	1.08 \pm 0.08	1.09 \pm 0.09	1.11 \pm 0.10	1.12 \pm 0.09
	AD	1.31 \pm 0.22***	1.31 \pm 0.16***	1.39 \pm 0.19***	1.45 \pm 0.23***	1.49 \pm 0.27***	1.62 \pm 0.38***	1.65 \pm 0.43***
Parietal	HC	0.98 \pm 0.04	0.98 \pm 0.06	1.01 \pm 0.06	1.03 \pm 0.06	1.04 \pm 0.06	1.04 \pm 0.08	1.05 \pm 0.09
	AD	1.39 \pm 0.37***	1.36 \pm 0.28***	1.45 \pm 0.33***	1.53 \pm 0.40***	1.59 \pm 0.47**	1.79 \pm 0.70***	1.84 \pm 0.77**
Posterior cingulate	HC	0.98 \pm 0.10	1.08 \pm 0.11	1.07 \pm 0.13	1.03 \pm 0.13	0.97 \pm 0.14	0.83 \pm 0.17	0.72 \pm 0.15
	AD	1.56 \pm 0.57***	1.64 \pm 0.46***	1.73 \pm 0.56***	1.82 \pm 0.68***	1.84 \pm 0.78***	1.88 \pm 1.13**	1.86 \pm 1.15*

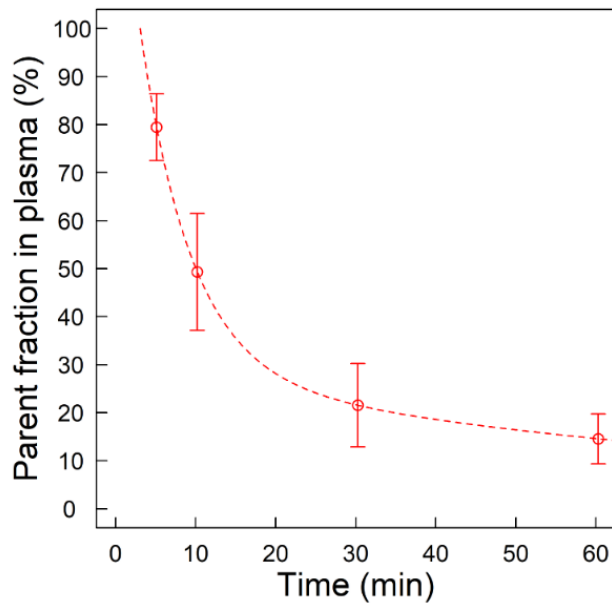
n.s. ($p > 0.05$), * ($p \leq 0.05$), ** ($p \leq 0.01$), ***: ($p \leq 0.001$)

Supplemental Table 2. Comparison of DVR and SUVR values in subcortical regions in AD and HC subjects and regions without tau deposition (cortex of HCs). SUVR values (mean \pm SD) and p-values[†] in HC and AD subjects are shown from different imaging windows for the whole cerebral cortex, pallidum, thalamus, striatum, subcortical white matter and choroid plexus.

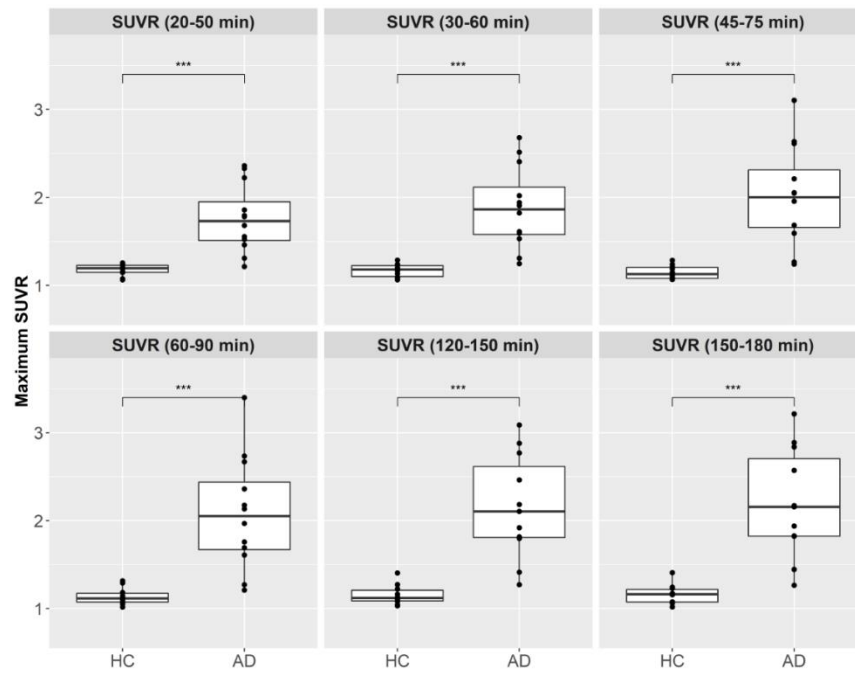
		NI-LGA		SUVR				
		DVR	20-50 min	30-60 min	45-75 min	60-90 min	120-150 min	150- 180 min
Cortex‡	HC	1.00 \pm 0.05	1.01 \pm 0.06	1.04 \pm 0.07	1.05 \pm 0.08	1.06 \pm 0.08	1.06 \pm 0.08	1.06 \pm 0.08
Pallidum	HC	0.97 \pm 0.11	1.11 \pm 0.15	1.05 \pm 0.16	0.95 \pm 0.17	0.88 \pm 0.16	0.73 \pm 0.14	0.65 \pm 0.11
	AD	1.09 \pm 0.10*	1.29 \pm 0.14***	1.21 \pm 0.15***	1.10 \pm 0.14	1.03 \pm 0.14	0.90 \pm 0.15	0.84 \pm 0.15
Thalamus	HC	1.00 \pm 0.08	1.04 \pm 0.10	0.99 \pm 0.11	0.93 \pm 0.11	0.90 \pm 0.12	0.77 \pm 0.11	0.72 \pm 0.10
	AD	0.98 \pm 0.05	1.04 \pm 0.08	0.99 \pm 0.08	0.96 \pm 0.07	0.93 \pm 0.07	0.85 \pm 0.08	0.80 \pm 0.07
Striatum	HC	0.86 \pm 0.08	0.94 \pm 0.10	0.90 \pm 0.10	0.83 \pm 0.10	0.78 \pm 0.11	0.66 \pm 0.09	0.59 \pm 0.09
	AD	1.01 \pm 0.10	1.11 \pm 0.10**	1.08 \pm 0.12	1.02 \pm 0.14	0.97 \pm 0.16	0.88 \pm 0.17	0.84 \pm 0.18
Subcortical white matter	HC	0.76 \pm 0.05	1.09 \pm 0.07*	1.09 \pm 0.09	1.01 \pm 0.11	0.90 \pm 0.10	0.63 \pm 0.10	0.55 \pm 0.08
	AD	0.81 \pm 0.08	1.13 \pm 0.13**	1.14 \pm 0.12**	1.07 \pm 0.12	0.97 \pm 0.12	0.70 \pm 0.11	0.62 \pm 0.11
Choroid plexus	HC	0.96 \pm 0.12	1.09 \pm 0.16	1.09 \pm 0.16	1.07 \pm 0.14	1.03 \pm 0.14	0.90 \pm 0.12	0.88 \pm 0.13
	AD	0.83 \pm 0.21	0.91 \pm 0.25	0.95 \pm 0.26	0.97 \pm 0.27	0.97 \pm 0.27	0.94 \pm 0.20	0.93 \pm 0.20

[†] p-values were calculated using a Mann-Whitney U test (unilateral test, H_0 : SUVR = SUVR(cortex), H_1 : SUVR > SUVR(cortex)) are obtained from the comparison of SUVRs in the cortex from HC to pallidum, thalamus, striatum, subcortical white matter (centrum semiovale) and choroid plexus.* ($p \leq 0.05$), ** ($p \leq 0.01$), ***: ($p \leq 0.001$)

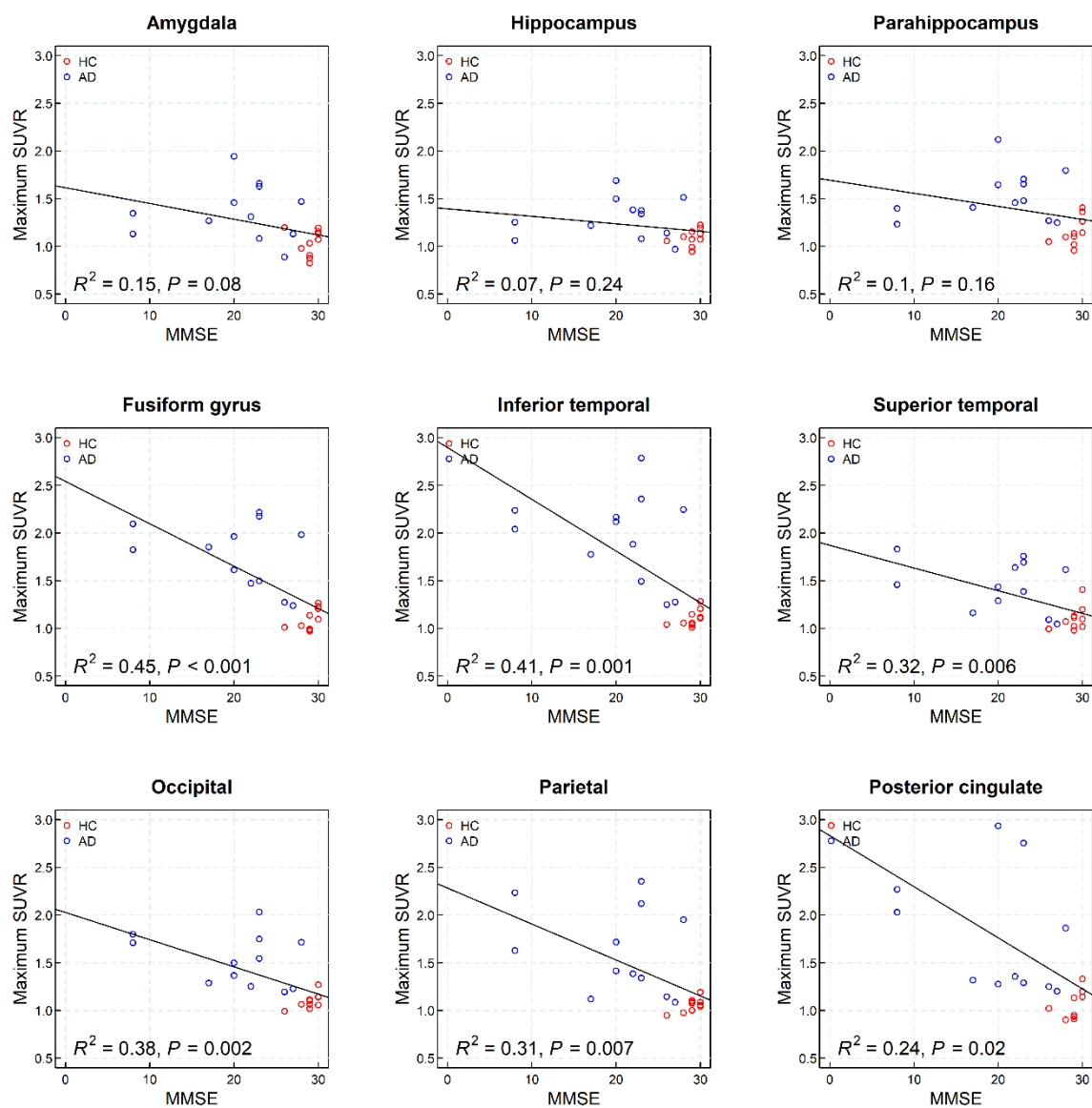
‡ SUVR in the cortex was calculated as the volume-weighted average of the SUVR in the amygdala, hippocampus and, parahippocampus, fusiform gyrus, inferior temporal cortex, superior temporal cortex, occipital cortex, parietal cortex and posterior cingulate cortex.



Supplemental Figure 1. The parent fraction in venous plasma over time was described with a biexponential function with the following parameters: $\alpha=72.01$, $\tau_1=6.38$ min, $\tau_2=87.15$ min, $t_0 = 3.23$ min.



Supplemental Figure 2. Boxplot of maximum SUVR at each diagnosis group across different imaging windows. * ($p \leq 0.05$), ** ($p \leq 0.01$), ***: ($p \leq 0.001$)



Supplemental Figure 3. Correlation analysis of ^{18}F -PI-2620 uptake at 45-75 min p.i. in individual brain regions (maximum SUVR from the left or the right hemisphere) and MMSE.